International Journal of Nanomedicine

Dovepress
Taylor & Francis Group

Open Access Full Text Article

ORIGINAL RESEARCH

Lipid-Engineered Small-Sized Metal-Organic Frameworks for Targeted Delivery of Anlotinib in Lung Cancer Treatment

Chao Fang[1,*], Daihan Xie[1,*], Fanlei Kong[2,*], Xin Yu[1], Jingting Yin[1], Yu Huo[3], Chunxia Su[1]

[1]Department of Comprehensive Oncology Center, Shanghai Pulmonary Hospital, Tongji University Medical School Cancer Institute, School of Medicine, Tongji University, Shanghai, 200433, People's Republic of China; [2]Department of Ultrasound in Medicine, Second Affiliated Hospital, Zhejiang University School of Medicine, Hangzhou, Zhejiang Province, 310009, People's Republic of China; [3]Faculty of Chinese Medicine Science, Guangxi University of Chinese Medicine, Nanning, Guangxi Zhuang Autonomous Region, 530222, People's Republic of China

*These authors contributed equally to this work

Correspondence: Chunxia Su, Department of Comprehensive Oncology Center, Shanghai Pulmonary Hospital, Tongji University Medical School Cancer Institute, School of Medicine, Tongji University, No. 507 Zheng-min Road, Shanghai, 200433, People's Republic of China, Email susu_mail@126.com; Yu Huo, Faculty of Chinese Medicine Science, Guangxi University of Chinese Medicine, No. 13 Wu-He Avenue, Nanning, 530222, Guangxi Zhuang Autonomous Region, People's Republic of China, Email huoyu_10@163.com

Purpose: In this study, we report the design and evaluation of Anlo@MOF-Lipo (AML), a liposome coated, small sized MIL-101(Fe) metal-organic framework (MOF) for targeted delivery of the multi target tyrosine kinase inhibitor anlotinib in lung cancer treatment.
Methods: In detail, the biomimetic liposome shell enhances nanoparticle biocompatibility, while the MIL-101(Fe) core enables pH responsive release of Fe^{3+} under acidic tumor conditions, triggering Fenton-like reactions and generating cytotoxic reactive oxygen species. Anlotinib is encapsulated within the MOF pores for sustained, intratumoral release, suppressing the growth of tumors.
Results: Characterization confirmed uniform liposome coating and sustained anlotinib release of AML. In vitro, AML demonstrated superior cellular uptake and cytotoxicity in lung cancer cells. In a murine subcutaneous tumor model, AML treatment achieved a greater tumor volume reduction than free anlotinib, with no observable systemic toxicity. Furthermore, in the orthotopic lung cancer model, AML achieved the most pronounced therapeutic efficacy among all treatment groups.
Conclusion: This dual mode therapeutic strategy-combining targeted chemotherapy with oxidative stress induction-highlights the potential of AML as a promising nanomaterial for improving lung cancer treatment.
Keywords: anlotinib, fenton-like reaction, lung cancer, metal-organic framework, targeted therapy

Introduction

Lung cancer is a highly malignant neoplasm that typically originates in the bronchi or lung parenchyma.[1–4] As one of the leading causes of cancer-related mortality worldwide, it claims millions of lives each year.[5,6] Due to the absence of typical early symptoms, over 70% of patients are diagnosed at advanced stages, resulting in low curability and poor prognosis.[7] This not only imposes a significant psychological burden on patients but also leads to substantial social and economic pressures. Currently, the treatment modalities for lung cancer primarily include surgical resection, radiation therapy, chemotherapy, and targeted therapy.[8,9] However, these modalities continue to face numerous challenges.[10,11]

In recent years, targeted therapy has achieved substantial progress in lung cancer management.[12,13] Anlotinib, an oral multi-target tyrosine kinase inhibitor, has demonstrated clinical efficacy in treating advanced non-small cell lung cancer (NSCLC), small cell lung cancer (SCLC), and several other malignancies.[14–18] Despite these benefits, its therapeutic potential remains limited by poor aqueous solubility, short plasma half-life and off-target toxicity.[19–21] These pharmacokinetic and safety constraints highlights the urgent need for the development of an efficient delivery system to enhance its clinical application.

https://doi.org/10.2147/IJN.S566873
Received: 11 September 2025
Accepted: 6 January 2026
Published: 15 January 2026

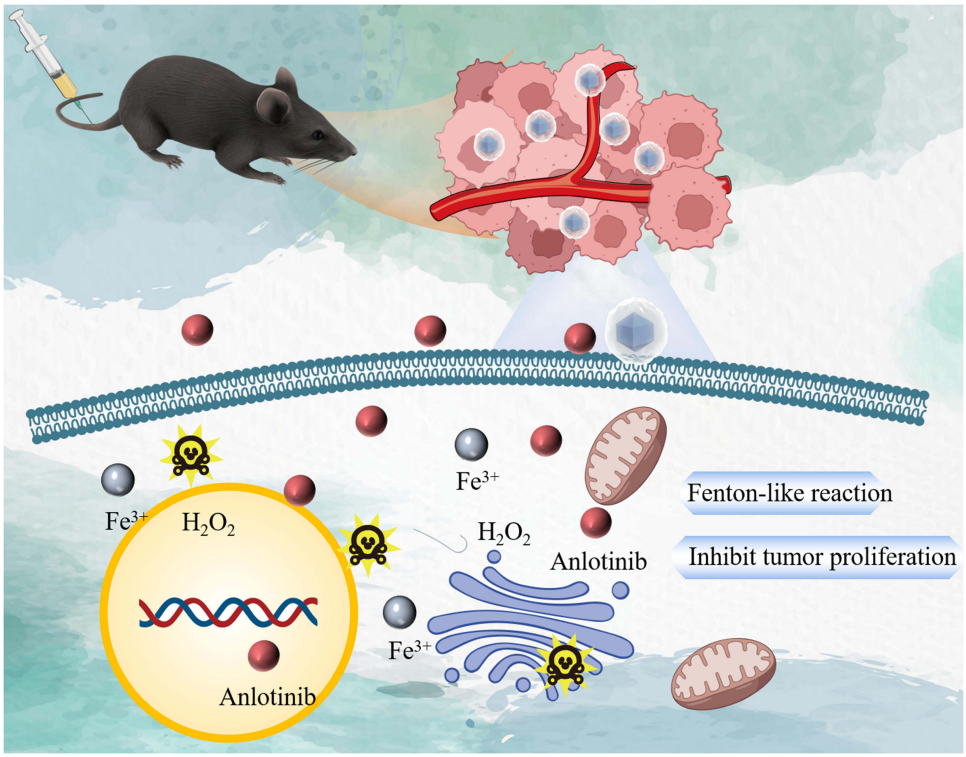

Figure 1 Schematic diagram. The diagram illustrating the AML administration via tail vein injection and its tumor-targeting mechanism through the EPR effect (upper) and the anti-cancer mechanism of AML at the tumor site (lower). Specifically, AML is taken up by tumor cells, releasing anlotinib and Fe^{3+}. Anlotinib inhibits tumor cell proliferation, while Fe^{3+} induces ROS generation via Fenton reaction, promoting tumor cell death.

At the same time, the development of nanodrug delivery systems has provided new strategies for improving the efficacy of anti-cancer drugs and reducing side effects. Metal-organic frameworks (MOFs) as a new type of porous materials, show great potential in drug delivery due to their high specific surface area, adjustable pore size and good biocompatibility.[22–24] However, traditional MOF materials (typically larger than 300 nm) face limitations in tumor targeting and cell uptake efficiency.[25] To address these challenges, researchers are working to develop smaller-sized MOF materials (approximately 100 nm) to optimize drug delivery performance.

In this study, we designed and synthesized a novel nanodrug delivery system based on the iron-based metal-organic framework MIL-101(Fe) by solvothermal synthesis. Compared with conventional MOF materials, MIL-101(Fe) exhibits a smaller size (~100 nm) and is surface-modified with a liposomal surface to improve its biocompatibility and stability. This design not only enables efficient loading and delivery of anlotinib, but also leverages the ability of MIL-101(Fe) to release Fe^3+ in the tumor microenvironment, generating reactive oxygen species (ROS) through Fenton-like reactions to augment tumor cell damage (Figure 1). Our results demonstrate that this novel Anlo@MOF-Lipo (AML) system, integrating sustained anlotinib delivery with MOF-mediated oxidative stress—offers a promising strategy to enhance antitumor efficacy while reducing systemic toxicity.

Materials and Methods

Reagents and Cells

Dimethyl sulfoxide (DMSO), ethyl alcohol, PBS, DPPC, $FeCl_3$•$6H_2O$, DSPE-PEG2000-NHS, benzene-1,4-dicarboxylic acid (H2BDC), anlotinib, N,N-dimethylformamide (DMF) and $NaHCO_3$ reagents were purchased from Shanghai Aladdin Biochemical Technology Co., Ltd. (Shanghai, China). Enzyme-linked immunosorbent assay (ELISA) kits for CRP, TNF-α, IL-6, IL-10, an iron ion test kit, an Annexin V-FITC apoptosis detection kit, a mitochondrial membrane potential assay kit with JC-1, a reactive oxygen species (ROS) assay kit, a cell counting kit-8 (CCK-8), and DAPI for nuclear staining were purchased from Beyotime Biotechnology Co., Ltd. (Shanghai, China). A cTnI ELISA kit was

purchased from Elabscience Biotechnology Co., Ltd. (Wuhan, China). All biochemical reagents were used without further purification. Lewis lung carcinoma (LLC) cells were purchased from ATCC and cultured in DMEM supplemented with 10% fetal bovine serum, penicillin (100 IU/mL) and streptomycin (100 μg/mL). Other chemicals used were purchased from Aladdin Biochemical Technology Co., Ltd.

Animals

Four-week-old female C57 mice were obtained from Slack Laboratory Animals Co., Ltd. (Shanghai, China) and housed in specific-pathogen-free (SPF) conditions. All the experiments on live mice were approved by the Committee on Animals of Guangxi University of Chinese Medicine.

Synthesis of MIL-101(Fe)

In a typical procedure, 2.5 mmol of $FeCl_3$•$6H_2O$ and 3.75 mmol of H2BDC were dissolved in 30 mL of DMF. The mixture was stirred for 15 min and then heated at 70 °C for 10 h. After reacting, the final products were centrifuged (8000×g for 10 minutes) and washed with 2 mL ethanol three times and with 2 mL distilled water three times.[26]

Synthesis of Anlo@MOF

To load anlotinib into the pores of MOFs, we dispersed synthetic MIL-101(Fe) (10 mg) into 2 mL of 1×PBS solution containing 10 mg of anlotinib and the resulting mixture was then stirred for 24 h at 37 °C. The products (Anlo@MOF) were centrifuged (8000×g for 10 minutes) and washed with distilled water three times to remove the free anlotinib.

Synthesis of Anlo@MOF-Lipo

10 mg Anlo@MOF was dispersed in 5 mL chloroform. After complete dispersion, 15 mg DPPC and 30 mg DSPE-PEG2000-NHS were added and evenly dispersed in the Anlo@MOF solution in chloroform via sonication. After that, the mixture was rotated and evaporated at 37 °C for 30 minutes using a rotary evaporator. The product (AML) was collected via high-speed centrifugation at 8000×g for 10 min at room temperature. The centrifuged products were collected, dispersed with 5 mL anhydrous ethanol and centrifuged at 8000×g for 10 min at room temperature. This step was repeated three times. AML was incubated with amino-Cy5.5 or DiD dye under thorough mixing, followed by centrifugation. The pellet was washed with 5 mL of 1×PBS and centrifuged at 8000×g for 10 min at room temperature for three times. The pellet was redispersed in 5 mL PBS and AML products were obtained through a hand-pushed micro-liposome extruder (Hamilton, USA). Solid AML was then collected by centrifugation and dried.

Characterization

Transmission electron microscopy (TEM) images were captured using a Hitachi H-8100EM system (Tokyo, Japan) with an accelerating voltage of 75 keV and a magnification of 100,000×. Scanning electron microscope (SEM) images were obtained from a Hitachi S-4800 FE-SEM (Tokyo, Japan) system at a magnification of 50,000×. Size distribution and zeta potential of the nanomaterials were measured by dynamic light scattering (DLS) using a ZEN 3600 system (Malvern Instruments, Worcestershire, United Kingdom), with samples prepared at a concentration of 0.1 mg/mL, pH 7.0, and measured at room temperature. UV/vis absorption spectra were obtained from a Cary 3500 spectrometer (Agilent Santa Clara, California) with the baseline calibrated using distilled water and a wavelength range of 200–800 nm.

Measurement of Ultraviolet Absorption Spectrum of Anlotinib

The ultraviolet (UV) absorption spectra of anlotinib solutions at different concentrations were measured using a UV–Vis spectrophotometer to establish a standard calibration curve based on the characteristic absorption peak at 218 nm. Prior to the experiment, a series of anlotinib standard solutions with concentrations of 0.8, 4, 20, 100, and 500 μg/mL were prepared in phosphate-buffered saline (PBS) through stepwise dilution. All solutions were freshly prepared and used immediately to prevent degradation. Quartz cuvettes were cleaned with pure PBS three times prior to measurement. Baseline correction was performed using PBS as the blank. Standard solutions were sequentially loaded from low to high concentration, and the outer surface of the cuvettes was wiped clean before insertion into the sample chamber. The

absorption spectra were scanned over the wavelength range of 200–600 nm, with emphasis on the peak at 218 nm. Absorbance values at 218 nm were recorded for each concentration, and each measurement was performed in triplicate to minimize random error. A calibration curve was constructed by plotting the average absorbance at 218 nm versus anlotinib concentration. Linear regression analysis was performed using the least-squares method, and the regression equation and correlation coefficient (R^2) were determined to evaluate the reliability of the linear relationship, providing a basis for subsequent quantitative analyses.

Drug Release of Anlotinib in AML

Three AML samples (50 mg each) were dispersed in 1 mL of PBS buffer at pH 5.5, 6.5, and 7.4, respectively. The dispersions were incubated at 37 °C with constant stirring at 60 rpm to maintain uniform suspension. Drug release was monitored at predetermined time points (1, 2, 3, 4, 5, 6, 7, and 8 h). At each time point, stirring was briefly paused to allow particle sedimentation, and a defined volume of the supernatant was collected using a micropipette.

The supernatants were analyzed using a preheated UV–Vis spectrophotometer, with PBS of the corresponding pH as the blank. Absorbance at 218 nm was recorded using quartz cuvettes with a 1-cm path length. The concentration of released anlotinib was calculated from the previously established standard curve. Cumulative release percentages were determined and plotted as a function of time for each pH condition. Comparative analysis of the release profiles allowed assessment of the influence of pH on the drug release behavior of AML formulations.

Electron Paramagnetic Resonance (EPR) Spectroscopy

The Fenton-like activity of Anlotinib-@MOF-Lipo (AML) under different pH conditions was assessed using electron paramagnetic resonance (EPR) spectroscopy (Bruker EMX). Phosphate-buffered solutions at pH 5.5, 6.5, and 7.4 were freshly prepared as reaction media. Hydrogen peroxide (H_2O_2) and 5,5-dimethyl-1-pyrroline N-oxide (DMPO) spin trap solutions were prepared immediately prior to use to ensure reagent activity. For each pH condition, equal amounts of AML were dispersed in the corresponding buffer. H_2O_2 and DMPO were then added sequentially to initiate the Fenton-like reaction. Following incubation at the predetermined temperature for a defined period, an aliquot of the reaction mixture was transferred into a quartz EPR flat cell using a micropipette and immediately inserted into the pre-adjusted resonant cavity of the Bruker EMX spectrometer. EPR measurements were performed at room temperature with the following instrument settings: central magnetic field, 3480 G; sweep width, 100 G; microwave power, 20 mW; modulation frequency, 100 kHz; and modulation amplitude, 1.0 G. Each pH condition was analyzed in triplicate to ensure reproducibility. The characteristic DMPO-OH quartet signal was recorded, and hydroxyl radical generation was quantified by analyzing the peak height or integrated peak area. This approach allowed systematic evaluation of the pH-dependent Fenton-like activity of AML and provided insight into the influence of environmental pH on hydroxyl radical generation.

AML Stability Verification

5 mg of AML was dispersed in 1.5 mL of DMEM, PBS, or ddH_2O in separate centrifuge tubes. The dispersions were visually observed and photographed at different time points. Size distribution and zeta potential of the nanomaterials were measured at the same time points using DLS.

Cell Experiment

LLC Cell Uptake of AML

LLC cells in the logarithmic growth phase were seeded at an appropriate density in confocal culture dishes for microscopic observation and simultaneously in parallel in standard culture plates for flow cytometry analysis. Prior to the uptake experiment, AML nanoformulations were labeled with the lipophilic dye DiD by co-incubation to embed the dye into the lipid layer, followed by centrifugation and purification to remove unbound dye, yielding DiD-labeled AML.

Cells were incubated with the respective formulations at 37 °C with 5% CO_2 for 1, 2, and 4 h. At each time point, the culture medium was carefully removed, and cells were washed three times with pre-cooled PBS to eliminate residual nanoparticles and extracellular dye. For confocal microscopy, cells were stained with DAPI-containing medium for nuclear labeling for 10 min, followed by washing with PBS. Confocal imaging was performed immediately, with blue

nuclear signals collected using the DAPI channel and red fluorescence from DiD captured in the corresponding channel. High-resolution images were reconstructed to visualize the intracellular localization and distribution of DiD-AML. For flow cytometry analysis, washed cells were detached with trypsin, resuspended in PBS, and immediately analyzed. Voltage and compensation settings were calibrated using unstained cells and free DiD controls. Fluorescence signals from at least 10,000 cells per sample were collected, and the proportion of DiD-positive cells and their mean fluorescence intensity were quantified using FlowJo software to assess the cellular uptake efficiency of AML nanoformulations at the designated time points.

Cell Proliferation Experiment

LLC cells in the logarithmic growth phase were seeded uniformly in 96-well plates at a density of 5×10^3 cells per well and incubated at 37 °C with 5% CO_2 for 24 h to ensure full adhesion. After attachment, cells were treated with serial dilutions of MOF, Anlo@MOF, or AML nanoformulations prepared in complete culture medium. The Control group received fresh medium only. Each treatment was performed in at least five replicate wells per concentration. Following incubation for the designated time points, 10 μL of CCK-8 solution was added to each well and incubated for 3 h. Absorbance at 450 nm was measured using a microplate reader, which correlates directly with the number of viable cells. Cell proliferation inhibition rates were calculated by comparing the absorbance values of each treatment group to those of the Control group.

ROS Detection

LLC cells in the logarithmic growth phase were seeded at an appropriate density in confocal microscopy dishes and incubated at 37 °C with 5% CO_2 for 24 h to allow complete adhesion. Following adhesion, the culture medium was aspirated and replaced with fresh medium containing MOF, Anlo@MOF, or AML nanoformulations. Different incubation time points were set for each group. Approximately 30 min prior to each predetermined time point, the medium was gently removed, and cells were washed twice with serum-free medium to remove residual nanoparticles. The DCFH-DA probe, diluted to the working concentration in serum-free medium, was added, and cells were incubated in the dark at 37 °C for 30 min. After incubation, cells were washed three times with serum-free medium to remove extracellular probe, and a small volume of fresh medium was added for immediate confocal imaging. Confocal microscopy settings were as follows: excitation at 488 nm (argon ion laser) and emission collection at 500–550 nm for oxidized DCF fluorescence; nuclear staining (if performed) was excited at 405 nm, with emission collected at 410–480 nm. Imaging parameters were kept identical across all groups. Fluorescence intensity per cell or per selected region was quantified using ImageJ, with at least three independent fields and over 30 cells analyzed per condition. Data were processed using GraphPad Prism and expressed as mean±SD. ROS levels in each treatment group at different time points were plotted as bar or line graphs to visualize the dynamics and relative intensities of ROS production induced by the nanoformulations.

Annexin V-mCherry Cell Apoptosis Detection

LLC cells in the logarithmic growth phase were seeded in confocal microscopy dishes at an appropriate density and incubated at 37 °C with 5% CO_2 for 24 h to achieve full adhesion. After adhesion, the culture medium was aspirated. The control group received fresh complete medium, while experimental groups were treated with medium containing MOF, Anlo@MOF, or AML nanoformulations and incubated for the designated time periods. At the end of each treatment, culture supernatants were aspirated, and cells were washed twice with pre-cooled PBS. Annexin V-mCherry staining solution was applied according to the manufacturer's instructions, and cells were incubated in the dark at room temperature for 30 min. Cells were then washed with Binding Buffer to remove unbound dye, and confocal imaging was performed immediately. Imaging parameters were set as follows: Annexin V-mCherry was excited at 561 nm, with red fluorescence collected at 570–620 nm; DAPI nuclear counterstaining was excited at 405 nm, with blue fluorescence collected at 410–480 nm. All imaging settings were kept consistent across groups. Apoptosis was evaluated by assessing the intensity and distribution of Annexin V-mCherry on the plasma membrane and its co-localization with nuclear staining. Semi-quantitative analysis of red fluorescence intensity in defined fields of view was performed using ImageJ to compare the relative apoptotic induction efficiency of the different nanoformulations.

Mitochondrial Membrane Potential (MMP) Assay

LLC cells in the logarithmic growth phase were seeded at an appropriate density in confocal microscopy dishes and incubated at 37°C with 5% CO_2 for 24 h to allow complete adhesion. After adhesion, the culture medium was aspirated and replaced with fresh medium containing MOF, Anlo@MOF, or AML nanoformulations, and cells were incubated for 24 h. Following treatment, cells were washed once with pre-cooled PBS and incubated with the JC-1 probe, diluted to the working concentration in serum-free medium, for 30 min at 37°C in the dark according to the manufacturer's instructions. After incubation, cells were washed twice with pre-warmed serum-free medium, and a small volume of PBS was added for immediate observation under a confocal microscope. The imaging parameters were set as follows: JC-1 aggregates (high mitochondrial membrane potential) were excited at 514 nm and emission was collected at 570–620 nm; JC-1 monomers (low mitochondrial membrane potential) were excited at 488 nm and emission was collected at 510–550 nm; Hoechst 33342 (if nuclear staining was performed) was excited at 405 nm and emission collected at 410–480 nm. All imaging conditions were kept consistent across groups. Red-to-green fluorescence intensity ratios were quantified using ImageJ, and at least three independent fields per sample were analyzed to semi-quantitatively assess mitochondrial membrane potential changes induced by different nanoformulations.

Enzyme-Linked Immunosorbent Assay (ELISA)

Whole blood samples from mice were collected and allowed to clot at room temperature for 30 min. Samples were centrifuged at 1000×g for 15 min at 4°C, and the serum was carefully collected to avoid hemolysis. Serum samples were aliquoted and stored at -80°C until analysis, avoiding repeated freeze-thaw cycles. Prior to the assay, serum samples, standards, and all kit components were equilibrated to room temperature for 1–2 h. The concentrated washing buffer was diluted 20-fold with ultrapure water according to the instructions. A 96-well microplate pre-coated with capture antibodies was loaded with gradient-diluted standards and appropriately diluted serum samples. Duplicate wells were set for each sample and standard, and blank control wells were included. Plates were gently tapped to mix, covered with a sealing film, and incubated at 37°C in the dark for 90 min. After incubation, wells were washed five times with washing buffer. Biotinylated detection antibody working solution was added to each well, followed by incubation at 37 °C for 60 min, and subsequent washing. Horseradish peroxidase-labeled streptavidin solution was then added and incubated at 37 °C for 30 min in the dark, followed by five additional washes. TMB substrate solution was added and incubated at 37 °C for 15–20 min until the standard wells developed a clear blue color. Stop solution was added to terminate the reaction, turning the solution yellow. Absorbance was measured at 450 nm, with 570 nm or 630 nm as reference wavelengths. A standard curve was generated using a four-parameter logistic (4-PL) model, with standard concentration as the x-axis and mean absorbance as the y-axis. Sample concentrations were calculated from the regression equation and adjusted by the dilution factor to determine the serum levels of CRP, TNF-α, IL-6, and IL-10.

Inductively Coupled Plasma Emission Spectrometry (ICP) Method

Tumor samples were dried and placed in digestion tubes. 10 mL of concentrated nitric acid was added and heated at 200°C for digestion. After complete evaporation, the sample was transferred to a 10 mL volumetric flask and diluted with 1% nitric acid. Following microwave digestion process, the iron content was detected using an ICP emission spectrometer (Optima 3000, Perkin Elmer, Norwalk, CT) based on standard iron solution calibration. Iron content was expressed as the proportion of the injected dose (tumor iron content/injected dose). Additionally, mouse blood was collected and the blood iron concentration determined by ICP was used to reflect systemic drug levels.

Ki-67 Mouse Tumor Tissue Immunohistochemistry

Tumor tissues were immediately fixed in 4% paraformaldehyde at 4°C for 24 hours, dehydrated through a graded ethanol series, cleared in xylene, and embedded in paraffin at 60°C for 2 hours. Paraffin-embedded blocks were sectioned at 4–5 μm thickness and mounted on glass slides. Sections were baked at 60°C for 1–2 hours to enhance adhesion, deparaffinized in xylene, and rehydrated through a descending ethanol series to deionized water. Antigen retrieval was performed using 0.01 M sodium citrate buffer (pH 6.0) in a microwave. After cooling, sections were washed with PBS and incubated with 3% hydrogen peroxide to block endogenous peroxidase activity, followed by serum blocking for 30 minutes. Sections were then incubated with Ki-67 primary antibody at 4°C overnight. After washing, HRP-conjugated secondary antibody was applied at room temperature for

30–60 minutes. The colorimetric reaction was developed using freshly prepared DAB solution and stopped upon appearance of a brown signal. Sections were counterstained with hematoxylin, differentiated, blued, dehydrated through graded ethanol, cleared in xylene, and mounted with neutral resin. Microscopic observation was performed to evaluate Ki-67 expression.

ROS Staining of Mouse Tumor Tissue

The tumor tissue was rapidly frozen and then cut into 4 - 5 micrometer thick slices. Sections were incubated with the ROS probe working solution at 37°C for 30 minutes in the dark, followed by PBS washing three times for 5 minutes each. Sections were mounted with anti-fade mounting medium and sealed with cover glasses. ROS signals were observed under CLSM.

H&E Staining of Mouse Tumor Tissue

Paraffin-embedded tumor sections (4–5 μm) were deparaffinized in xylene and rehydrated through a graded ethanol series to deionized water. Sections were stained in hematoxylin for 5–10 minutes, rinsed thoroughly with running tap water, and differentiated in 1% hydrochloric acid in 70% ethanol. Nuclei were blued in slightly alkaline water or PBS. Subsequently, sections were stained with eosin for 1–2 minutes. After staining, sections were dehydrated through graded ethanol, cleared in xylene, and mounted with neutral resin. Slides were examined under an optical microscope to assess nuclear morphology, cytoplasmic characteristics, and overall tissue structure.

Animal Experiment

All animal procedures were approved by the Experimental Animal Ethics Committee of Guangxi University of Chinese Medicine (DW20230528-104) and were performed in accordance with the Guide for the Care and Use of Laboratory Animals published by the National Institutes of Health (NIH). Specifically, mice were euthanized by cervical dislocation under anaesthesia, which was induced by intraperitoneal injection of 3% sodium pentobarbital at a dose of 30 mg/kg body weight. After injection, no discomfort of mice was observed. Death was confirmed by cessation of heartbeat and respiration. Tumor size was monitored daily and the maximum allowable tumor size was limited to 2000 mm^3. These procedures were applied consistently across both mouse models used in this study.

Twenty 4-week-old female C57 mice were randomly divided into four groups. Mice were housed separately. To establish the tumor model, LLC cells (1×10^6 cells/mL, 100 μL) were subcutaneously injected into the right thigh. Once tumors reached ~100 mm^3, drugs were administered via tail vein (performed blinded) every two days for 15 days. Cy5.5-labeled liposomes were used for in vivo imaging to evaluate biodistribution and clearance of nanomaterials by dissecting the heart, liver, spleen, lung and kidney and tumor. Tumor growth was monitored using a digital caliper, and volume was calculated as $V=0.5\times L\times W^2$. All mice were sacrificed at day 17, and tumors were excised, weighed, and processed for histopathology. Tumor tissue water content was determined by calculating the difference between the wet and dry weights, divided by the wet weight of the excised tumor samples, after drying at 60 °C until a constant weight was achieved. Blood cell analysis was performed using a blood cell analyzer (BC-5000Vet, Mindray).

Another twenty 4-week-old female C57 mice were used to establish an experimental lung metastasis model. LLC cells (1×10^6 cells/mL, 100 μL) were injected via the tail vein to induce pulmonary tumor nodules. Drug administration, imaging, and tissue analyses were conducted following the same protocol as in the subcutaneous model.

Statistical Analysis

All experiments were performed in triplicate using independent biological replicates. Data are presented as mean ±standard deviation (SD). Statistical comparisons between two groups were conducted using a two-tailed Student's *t*-test. Significance levels are indicated as follows: *P < 0.05, **P < 0.01, ***P < 0.001, and ****P < 0.0001.

Results

Synthesis and Characterization of AML

Figure 2a illustrates the synthesis scheme of AML. To characterize particle morphology and size, transmission electron microscopy (TEM) was performed on MIL-101(Fe). As shown in Figure 2b, MIL-101(Fe) exhibited a uniform particle

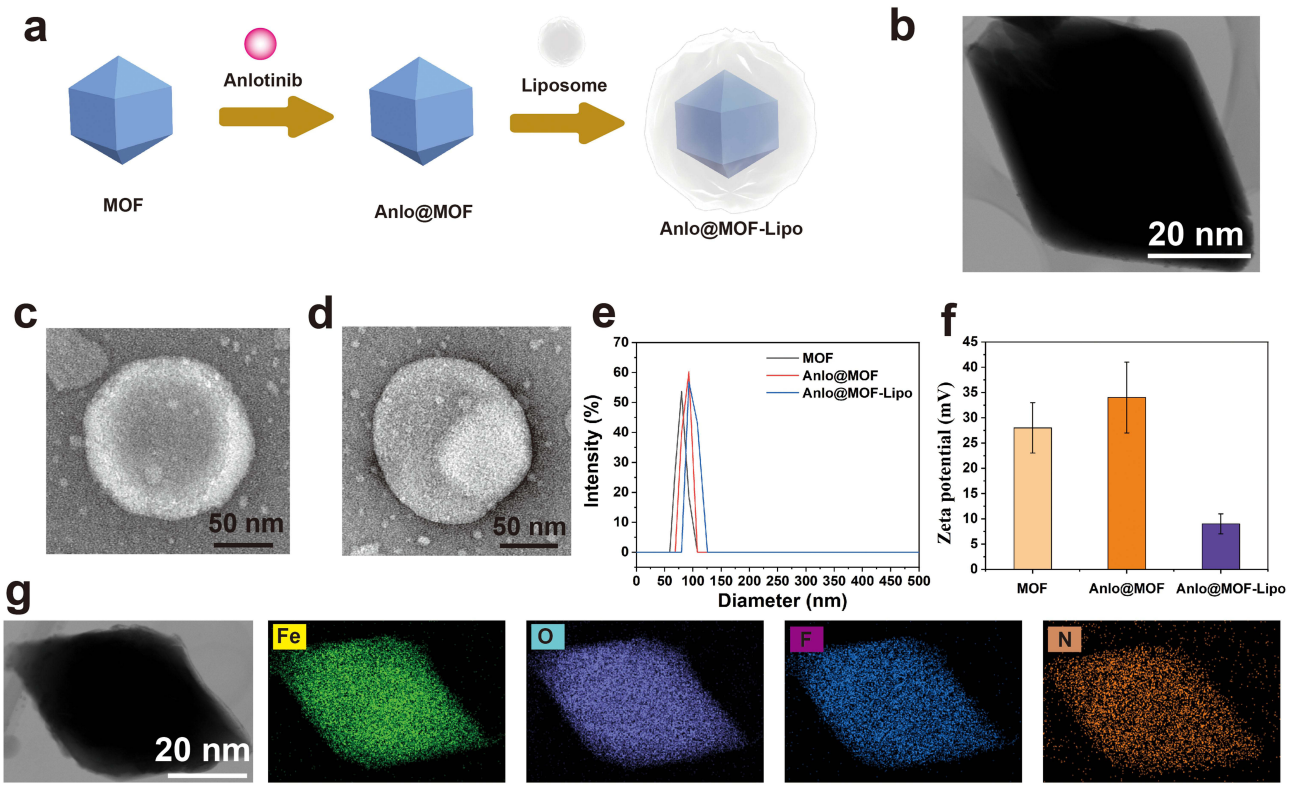

Figure 2 Synthesis and characterization of AML. (**a**) Schematic illustration of AML synthesis. (**b**) TEM image of MIL-101 (Fe). (**c**) TEM image of liposomes. (**d**) TEM image of AML. (**e**) Particle size distributions of different materials by DLS. (**f**) Surface potentials of different materials by Zetasizer. (**g**) SEM image and EDS (Fe, O, F, N) of AML. Data are presented as mean ± SD (n = 3).

size of approximately 60 nm. XRD, TGA, and Raman analyses of MIL-101(Fe) are presented in Figures S1-S3, respectively. Liposomes, composed of natural or synthetic phospholipids, have been widely applied in anti-cancer therapy owing to their ability to encapsulate drugs and deliver them to target sites via systemic circulation.[27–30] Their favorable biocompatibility, tunability, and sustained-release characteristics further enhance the efficacy and bioavailability of anti-cancer drugs.[31–34] TEM analysis of the liposomes and AML demonstrated that the synthesized liposomes effectively encapsulated MIL-101(Fe), forming a stable composite structure that prevented premature leakage (Figure 2c and d). Next, particle sizes were measured by dynamic light scattering (DLS). The results indicated that the organometallic framework ranged from 30–80 nm, and AML ranged from 50–110 nm (Figure 2e), providing additional evidence for the successful assembly of AML. In addition, zeta-potential measurements revealed a distinct surface charge shift after AML formation (Figure 2f), confirming the modification of surface properties. Energy-dispersive spectroscopy (EDS) confirmed the presence and distribution of Fe, O, F, and N elements within the nanocomposite, further validating the successful synthesis of AML (Figure 2g).

Extracellular Experiment of AML

To validate the loading of anlotinib within AML, UV absorption spectra were measured at a series of anlotinib concentrations (Figure 3a). The drug loading efficiency of anlotinib was 6.78% and the encapsulation efficiency was 69.65%. AML exhibited a sustained release profile in PBS at varying pH values, with accelerated release under acidic conditions that mimic the tumor microenvironment. The cumulative drug release continued for up to 8 hours (Figure 3b). Iron ion release was further assessed in corresponding buffer systems, showing a similarly accelerated release under acidic conditions and a sustained release duration lasting up to 10 hours (Figure 3c). Furthermore, the EPR spectra of AML at different pH values displayed a characteristic quartet signal, indicating the generation of hydroxyl radicals via Fenton-like reactions (Figure 3d). Notably, the signal intensity at pH 5.5 was higher than at pH 6.5 and 7.4, suggesting

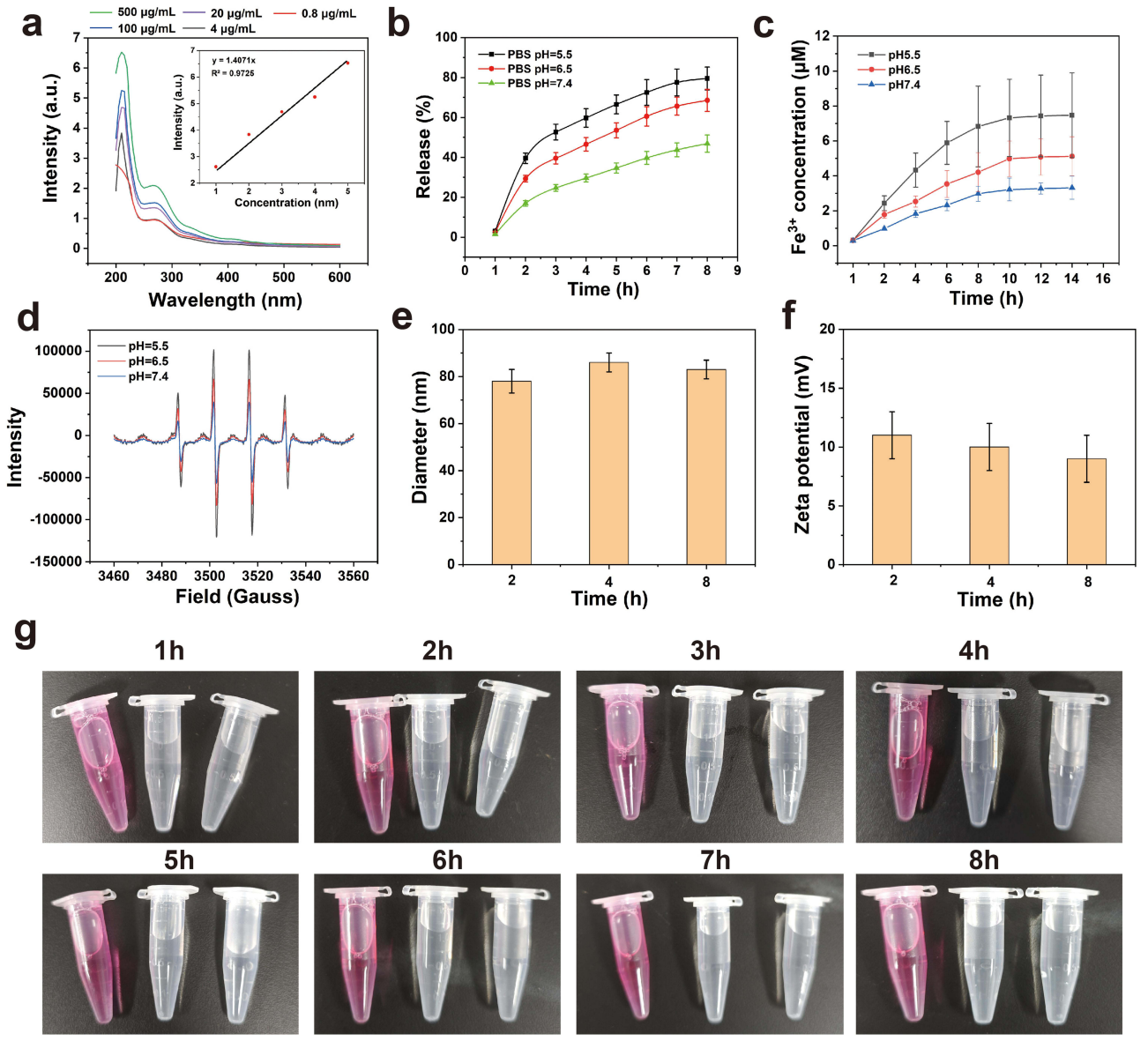

Figure 3 pH-responsive release and stability profiles of AML. (**a**) Ultraviolet absorption spectra of different concentrations of anlotinib and standard curves between anlotinib concentration and ultraviolet absorbance. (**b**) Time-dependent release curves of anlotinib from AML in buffers with different pH values. (**c**) Time-dependent release curves of Fe^{3+} from AML in buffers with different pH values. (**d**) EPR spectrum of AML in buffers with different pH values. (**e**) Particle sizes of AML by DLS at different time points. (**f**) Surface potentials of AML by Zetasizer at different time points. (**g**) Digital photographs of AML in DMEM, PBS, ddH2O at different time points. Data are presented as mean ± SD (n = 3).

that the acidic condition markedly promotes Fe^{3+} release and subsequent ROS production from MIL-101(Fe). No significant differences in size distribution or zeta potential were detected among 2, 4, or 8 hours (Figure 3e and f), indicating good stability during incubation. AML was also dispersed in DMEM, PBS, and ddH_2O to further validate storage stability (Figure 3g). No visible aggregation or precipitation was observed in any medium over prolonged storage to 8h. Collectively, these findings demonstrate the pH-responsive characteristics and excellent stability of the AML system.

In vitro Experiment of AML

To improve the potential for biomedical application, the cytotoxicity of AML was assessed using the standard CCK-8 assay to evaluate biocompatibility and safety.[35–38] The results showed that cytotoxicity was dependent on AML concentration, with the highest degree of cell death observed at 1000 μg/mL, suggesting a dose-dependent toxic effect

https://doi.org/10.2147/IJN.S566873

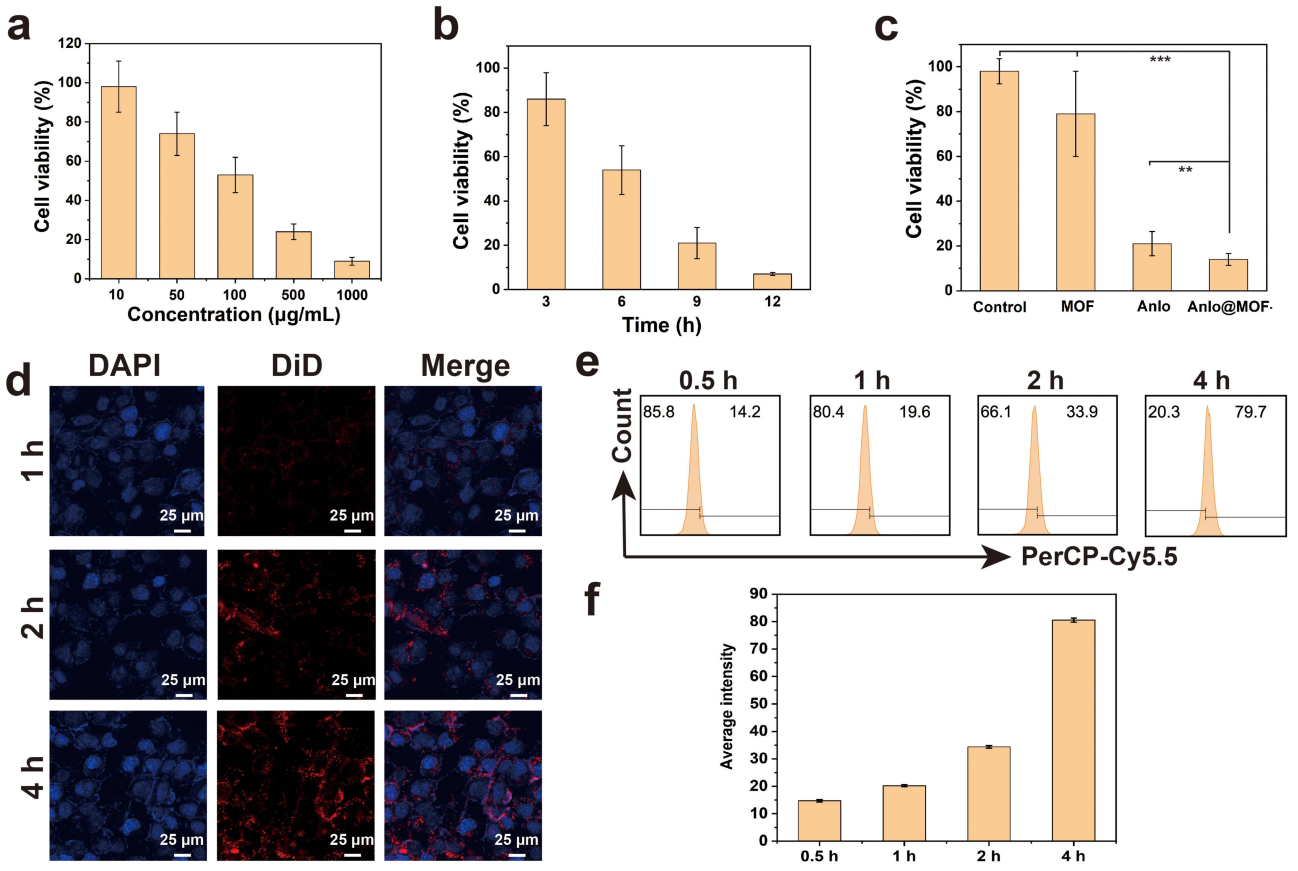

Figure 4 Cellular uptake and cytotoxicity of AML. (**a**) Cytotoxicity of AML in LLC cells after 6 h of incubation at various concentrations. (**b**) Cytotoxicity of AML (100 μg/mL) in LLC cells at different time points. (**c**) Cytotoxicity of different treatments (100 μg/mL) in LLC cells after 12 h of incubation. (**d**) CLSM images of LLC cells incubated with AML (100 μg/mL) at different time points. (**e**) Flow cytometry analysis of PerCP-Cy5.5-labeled AML internalization in LLC cells at different time points.(**f**) Quantification of mean fluorescence intensity in LLC cells at different time points. Data are presented as mean ± SD (n = 3). Statistical significance is indicated as follows: ** $P < 0.01$, *** $P < 0.001$.

(Figure 4a). After a prolonged incubation with AML at 100 μg/mL, a significant cytotoxic effect on LLC cells was still observed (Figure 4b). Moreover, among all material groups at an equal concentration of 100 μg/mL, AML exhibited the strongest cytotoxic effect (Figure 4c). These results suggest that AML has superior cytotoxic potency of AML compared with other formulations.

In order to visualize AML uptake, LLC cells were incubated with AML (100 μg/mL) for different durations. The results indicated that intracellular amount of AML (DiD, red) increased over time (Figure 4d), suggesting favorable interaction between AML and the cell, possibly facilitated by liposomal surface of AML. Flow cytometry analysis revealed a robust, time-dependent cellular uptake of the PerCP-Cy5.5 labeled AML, with the percentage of PerCP-Cy5.5-positive cells increasing from 14.2% at 0.5 h to 79.7% at 4 h (Figure 4e and f). Correspondingly, the average intracellular fluorescence intensity continuously rose over the monitored period, reaching its highest observed level after 4h, confirming substantial nanoparticle accumulation within cells.

To assess intracellular ROS production, confocal laser scanning microscope (CLSM) imaging was conducted on LLC cells treated with different material groups (100 μg/mL). Quantitive analysis showed pronounced ROS production in MOF-containing groups (Figure 5a and b). This finding supports that Fe^{3+} released from AML in a mildly acidic environment induces a Fenton-like reaction, thereby enhancing cytotoxicity. Further, time-dependent ROS generation was evaluated in LLC cells incubated with AML (100 μg/mL). The results showed that intracellular ROS increased with longer incubation times, further supporting ROS-inducing effect of AML (Figure 5c and d). In addition, apoptosis imaging was conducted across treatment groups. Following 3 h of incubation at 100 μg/mL, AML group exhibited the most pronounced apoptotic effect (Figure 5e and f). JC-1 staining revealed significant differences in mitochondrial

https://doi.org/10.2147/IJN.S566873

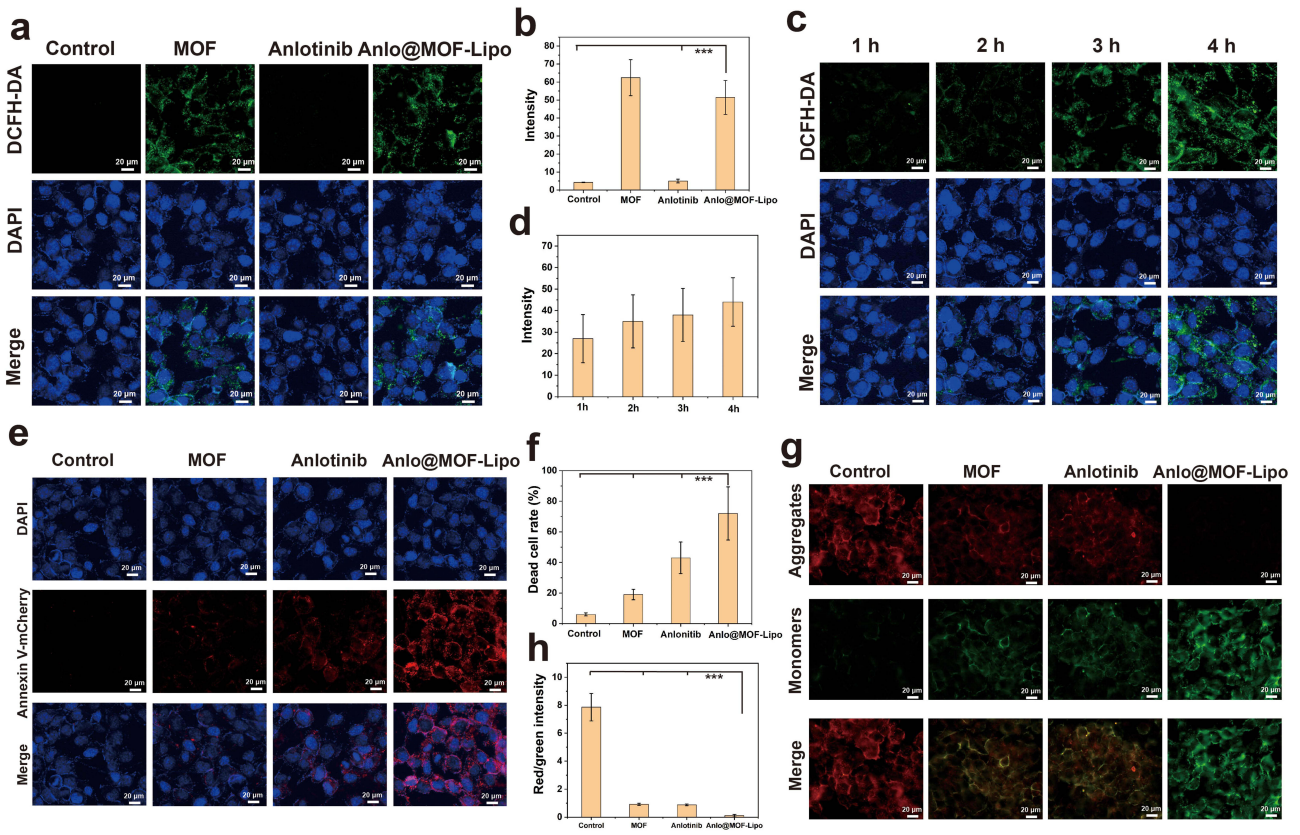

Figure 5 Intracellular ROS generation, apoptosis, and mitochondrial effects by AML. (**a**) CLSM images of intracellular ROS in each group (100 μg/mL, 6h). (**b**) Quantification of intracellular ROS levels shown in (**a**). (**c**) CLSM images of intracellular ROS with AML (100 μg/mL) at different time points. (**d**) Quantification of intracellular ROS levels shown in (**c**). (**e**) CLSM images of cell apoptosis in each group (100 μg/mL, 6h). (**f**) Quantification of cell apoptosis shown in (**e**). (**g**) CLSM images of MMP in each group (100 μg/mL, 6 h). (**h**) Quantification of MMP (indicated by ratio of red to green fluorescence intensity) shown in (**g**). Data are presented as mean ± SD (n = 3). Statistical significance is indicated as follows: *** P < 0.001.

membrane potential (MMP) among treatment groups (Figure 5g and h). Compared with MOF alone or anlotinib monotherapy, AML induced a more pronounced decrease in MMP, as indicated by a lower red/green fluorescence ratio. This suggests enhanced mitochondrial depolarization and apoptosis induction following AML treatment.

In vivo Experiment of AML

To investigate the anti-cancer efficacy of AML in vivo. LLC cells were implanted into the right thigh subcutaneously of the C57 mice. Once tumors reached approximately100 mm^3, PBS, MOF, anlotinib or AML (200 μg/mL, 200 μL each) was administered via tail vein injection every two days (Figure 6a). Biodistribution was assessed following Cy5.5-labeled AML administration. At 2 h post-injection, tumors in the AML group exhibited strong fluorescence, whereas no signal was detected in control mice. Comparable fluorescence intensities were observed in the liver and kidney (Figure 6b and c). These results suggest AML effectively accumulates at tumor sites via the enhanced permeability and retention (EPR) effect, confirming its tumor-targeting ability. Direct examination of excised tumors further demonstrated the therapeutic benefit of AML. Tumors from AML-treated mice were markedly smaller than those from other groups (Figure 6d). Quantitative tumor weight analysis showed that the AML group exhibited the lowest tumor mass and the slowest tumor growth rate (Figure 6e and f). The internal water content of tumor tissues significantly differed among treatment groups AML-treated tumors showing the lowest water content, consistent with reduced tumor burden (Figure 6g). Pharmacokinetic analysis revealed that the AML had the longest blood circulation half-life compared with either MOF or anlotinib alone (Figure 6h). The survival curves of mice were analyzed, and the mice in the AML group achieved the longest overall survival (Figure 6i). Body-weight monitoring further supported the therapeutic advantage of AML, as treated mice maintained relatively stable body weight throughout the study (Figure 6j-l). Tumor volume analysis showed

https://doi.org/10.2147/IJN.S566873

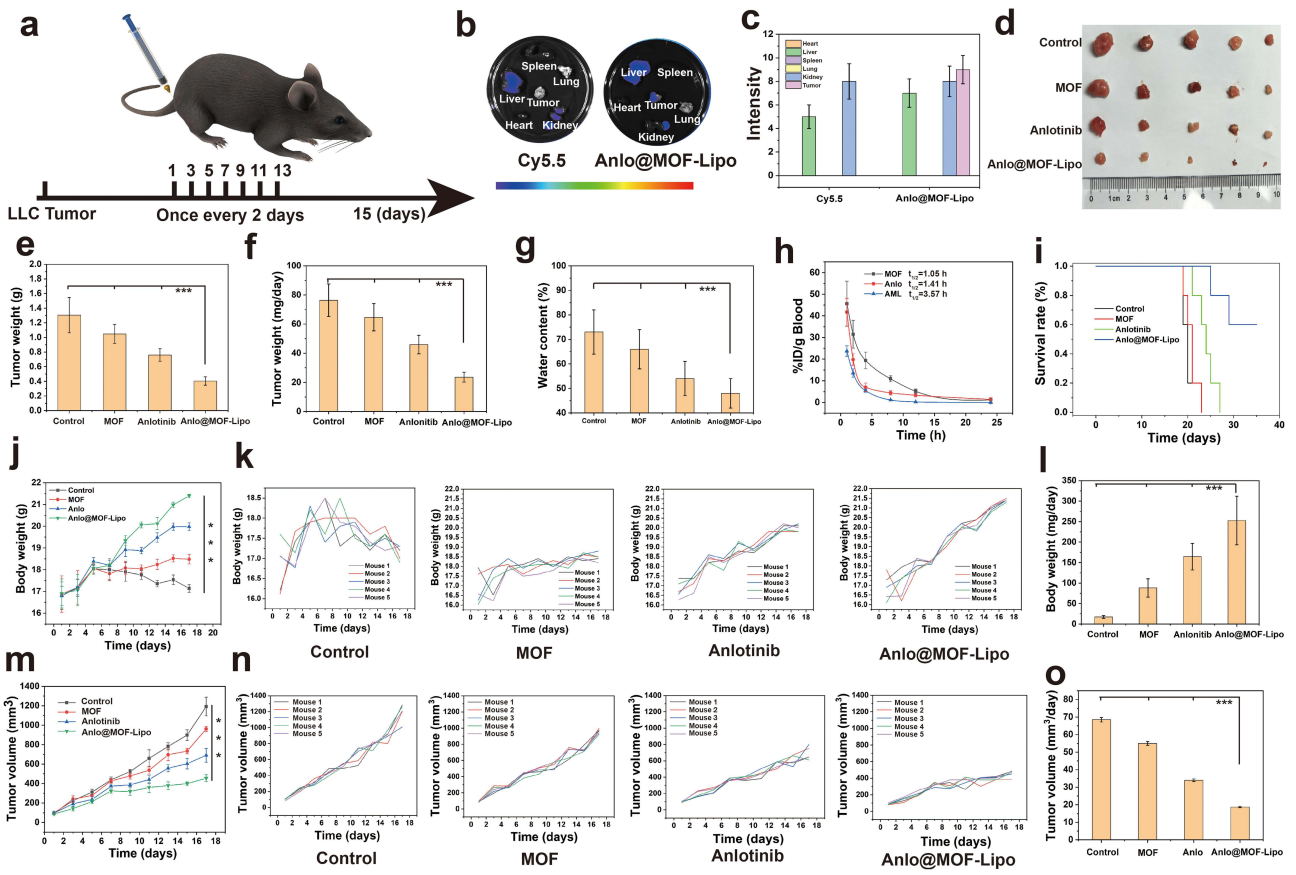

Figure 6 Biodistribution and anti-tumor efficacy of AML in subcutaneous models. (**a**) Treatment timeline for AML administration (200 μg/mL, 200 μL via tail vein injection). (**b**) Fluorescence imaging at 2 h post-injection to assess biodistribution of AML. (**c**) Quantification of fluorescence intensity shown in (**b**). (**d**) Images of excised tumors in each group. (**e**) Tumor weights in each group. (**f**) Changes in tumor weight in each group. (**g**) Water content of tumors in each group. (**h**) Blood concentrations and half-life of MOF, anlotinib, and AML after administration. (**i**) Survival analysis of mice with different treatments. (**j**) Average body weight changes across all groups. (**k**) Average body weight changes for each individual group. (**l**) Time-course changes in body weight in each group. (**m**) Average tumor volume changes across all groups. (**n**) Average tumor volume changes for each individual group. (**o**) Time-course changes in tumor volume in each group. Data are presented as mean ± SD (n = 5). Statistical significance is indicated as follows: *** $P < 0.001$.

rapid growth in the control group, whereas the AML group exhibited the smallest and slowest-growing tumors (Figure 6m-o). Iron content in tumor tissues was analyzed Tumors treated with MOF-containing materials showed higher intratumoral iron accumulation, indicating that a greater proportion of MOFs successfully reached the tumor sites (Figure 7a). Ki-67 staining showed AML exerted the most pronounced antiproliferative effect among all treatment groups (Figure 7b). Furthermore, ROS imaging confirmed that AML induced a substantial amount of ROS in tumor tissues (Figure 7c). To assess whether AML triggers hematotoxicity or immune response in vivo, blood cell counts and inflammation markers were measured. Two hours after tail vein injection of each material (200 μL, 200 μg/mL), blood samples were collected for analysis. No significant differences were observed in blood cell counts (Figure 7d-f), hemoglobin concentrations (Figure 7g) or inflammation markers (Figure 7h-k) between control and treated groups, suggesting AML does not cause hematotoxicity or induce acute inflammatory responses. Furthermore, hematoxylin and eosin (H&E) staining of major organs indicated no detectable pathological changes in any of the treatment groups (Figure 7l), providing additional evidence for the systemic safety of AML.

We next evaluated the biodistribution and therapeutic efficacy of AML system in a lung tumor model (Figure 8a). At 2 h post-injection, Cy5.5-labeled fluorescence signals were detected in the lungs of AML-treated mice, whereas no detectable signal was observed in the control group. (Figure 8b). Consistent with the subcutaneous tumor model, lung tumor nodules in AML-treated mice were markedly smaller than those from other groups (Figure 8c). In addition, lung weight and mouse body weight were recorded to evaluate the anti-cancer effects of AML (Figure 8d and e). Survival

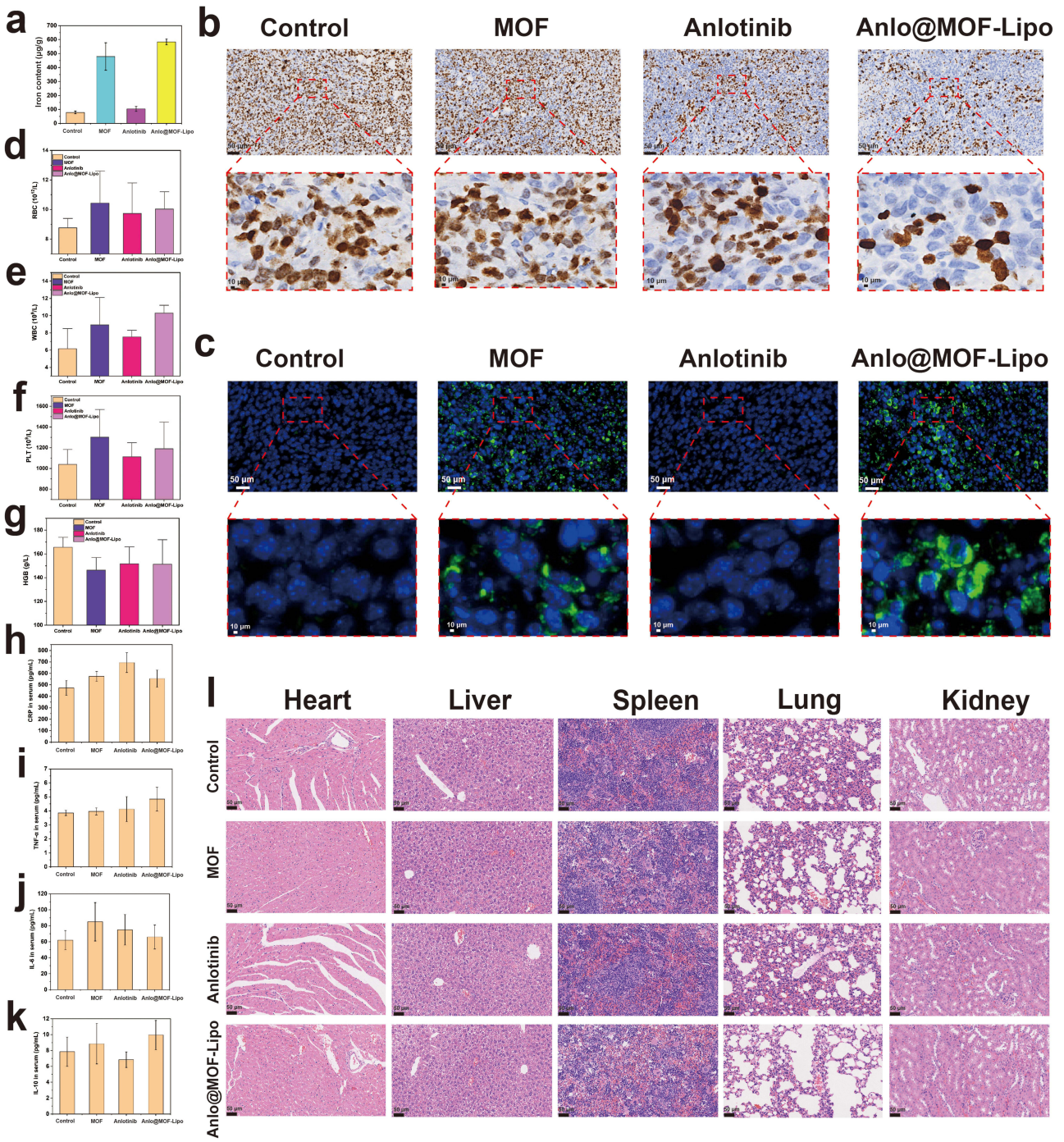

Figure 7 Mechanistic evaluation and biosafety of AML in tumor-bearing mice. (**a**) Iron content in tumor tissues by ICP in each group after 15 days of treatment. (**b**) Ki-67 staining of tumor tissues in each group after 15 days of treatment. (**c**) ROS staining of tumor tissues in each group after 15 days of treatment. (**d**) RBC (red blood cells) count measured 2 h after tail vein injection in each group. (**e**) WBC (white blood cells) count measured 2 h after tail vein injection in each group. (**f**) PLT (platelets) count measured 2 h after tail vein injection in each group. (**g**) HGB (hemoglobin) level measured 2 h after tail vein injection in each group. (**h**) Blood level of CRP measured 2 h after tail vein injection in each group. (**i**) Blood level of TNF-α measured 2 h after tail vein injection in each group. (**j**) Blood level of IL-6 measured 2 h after tail vein injection in each group. (**k**) Blood level of IL-10 measured 2 h after tail vein injection in each group. (**l**) H&E staining of heart, liver, spleen, lung and kidney after 15 days of treatment in each group. Data are presented as mean ± SD (n = 5).

analysis demonstrated that mice treated with AML exhibited the longest survival duration among all groups (Figure 8f). Given previous reports of anlotinib-induced cardiotoxicity, we monitored serum cTnI levels and performed H&E staining of heart tissues up to 5 weeks post-treatment. No significant histopathological abnormalities or elevation in cardiac bio markers were detected (Figure 8g and h).

https://doi.org/10.2147/IJN.S566873

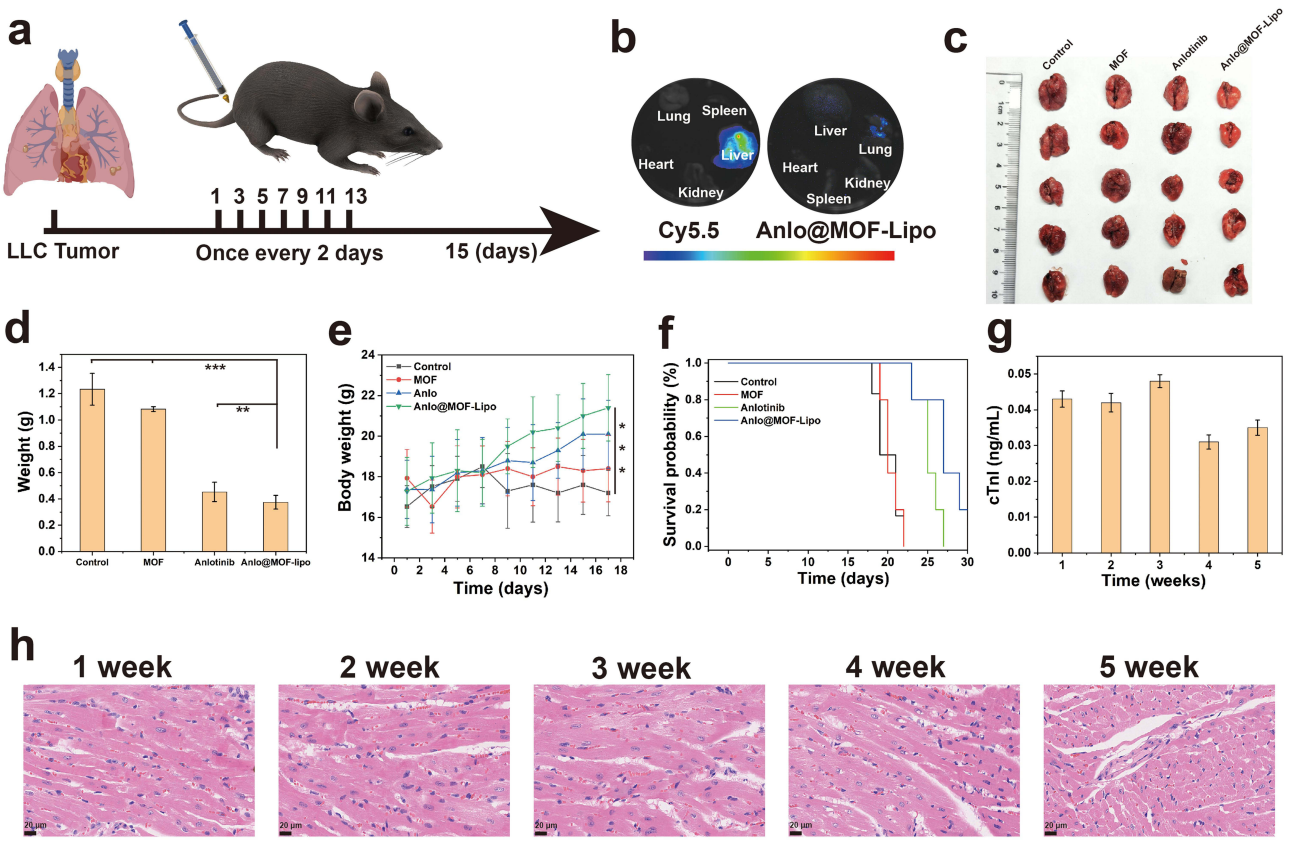

Figure 8 Anti-tumor efficacy and cardiac safety of AML in metastasis models. (**a**) Treatment timeline for AML administration (200 μg/mL, 200 μL via tail vein injection). (**b**) Fluorescence imaging at 2 h post-injection to assess biodistribution of AML. (**c**) Images of excised lung tissues in each group. (**d**) Lung weight in each group. (**e**) Average body weight changes in each group. (**f**) Survival analysis of mice with different treatments. (**g**) Serum levels of cardiac troponin I (c-TnI) measured at indicated time points after AML treatment. (**h**) H&E staining of heart tissues at indicated time points after AML treatment. Data are presented as mean ± SD (n = 5). Statistical significance is indicated as follows: *P < 0.05, ** P < 0.01, *** P < 0.001.

Discussion

In this study, we developed a novel strategy, Anlo@MOF-Lipo (AML), to enhance the delivery and therapeutic efficacy for lung cancer treatment. Compared with free anlotinib, the AML formulation significantly inhibited tumor growth and demonstrated superior intratumoral accumulation in vivo, highlighting the advantages of integrating size-engineered MOFs with liposomal surface modification.

The enhanced anti-tumor performance of AML can be largely attributed to the unique characteristics of small-sized MOFs. Their reduced dimensions facilitate deeper tumor penetration and more efficient utilization of the enhanced permeability and retention (EPR) effect, leading to improved biodistribution and intracellular uptake.[39–41] Additionally, the higher surface area-to-volume ratio enables increased drug loading and contributes to more controlled release behavior. However, small-sized MOFs also present several challenges, including reduced in vivo stability that leads to faster clearance and lower therapeutic efficacy.[26,42] Furthermore, excessively small MOFs may also introduce technical issues in large-scale production and raise safety concerns. Specifically, particles that are too small are prone to aggregation, exhibit poor drug-loading capacity, and are more readily cleared by the reticuloendothelial system. In contrast, the liposomal coating further stabilizes the MOF structure, reduces premature degradation, and improves systemic biocompatibility, collectively contributing to more sustained in vivo performance.

The sustained-release behavior of anlotinib observed in the AML system can be attributed to the combined structural characteristics of MIL-101(Fe) framework and the outer liposomal coating. The coordinated metal-ligand network of the MOF provides a confined structure that restricts molecular diffusion, while the liposomal layer further functions as a semi-permeable barrier, collectively slowing drug exchange with the surrounding medium. In addition, the mildly

acidic tumor-like environment promotes gradual MOF degradation, enabling stepwise release of both anlotinib and Fe^{3+} ions. These synergistic effects result in a release duration of approximately 8 hours, which falls within the expected kinetic range reported for similar MOF-based or MOF-liposome hybrid formulations.[43,44] Although the in vitro release profile of AML shows a relatively short drug release period, this does not directly translate to its in vivo pharmacokinetics. In biological systems, drug biodistribution is influenced by tissue distribution, protein binding, endocytosis, and nanoparticle retention, all of which substantially prolong effective drug exposure. The MOF–liposome hybrid structure further facilitates EPR-mediated tumor accumulation and extended retention in tumor tissue, enabling sustained intracellular release after blood concentrations begin to decline. In addition, the release of Fe^{3+} and subsequent Fenton-like ROS generation provides a secondary, longer-lasting therapeutic effect that is not solely dependent on continuous anlotinib release. Consistent with this mechanism, our pharmacokinetic data show a gradual decline in plasma concentration with a relatively stable residual level maintained beyond 12 h, supporting the rationale for a 48 h dosing interval despite the shorter in vitro release duration.

AML treatment induced significantly higher apoptosis rates. Furthermore, JC-1 staining revealed a pronounced disruption of mitochondrial membrane potential following AML treatment compared to anlotinib monotherapy, indicating mitochondrial dysfunction. This mitochondrial impairment likely serves as a key mechanistic link explaining how ROS potentiates the therapeutic effect of anlotinib in tumor cells.

However, this study has certain limitations that require further investigation. First, safety assessment was limited, as known adverse effects of anlotinib, such as hypertension, were not specifically monitored in our animal experiments. Nonetheless, during the 5-week treatment period, no signs of acute distress or mortality were observed in the AML-treated group, indicating a favorable preclinical safety profile. Second, detailed pharmacokinetic profiling was not performed, which is important for understanding the in vivo behavior and distribution of the MOF-based delivery system. Third, although both subcutaneous and metastatic tumor models were employed, they were generated using the same LLC cell line in C57BL/6 mice. As a result, the findings may not fully reflect the biological heterogeneity of human tumors or account for inter-species differences in metabolism and immune responses. Finally, the study focused on a specific MOF-based delivery system, and future investigations should explore combinations with other therapeutic agents and cancer types to expand the applicability of this platform. Regarding clinical implications, the combination of this delivery system with immunotherapy may further enhance antitumor efficacy. For potential clinical translation, optimization of production processes, dosing strategies, and long-term safety evaluations will be essential. Overall, this platform provides a promising strategy for targeted drug delivery, which may improve therapeutic efficacy while minimizing systemic toxicity in lung cancer patients.

Conclusion

In summary, we developed a novel strategy for the delivery of anlotinib based on small-sized MOFs for lung cancer therapy. The reduced particle size facilitated tumor penetration and cellular uptake, while biomimetic liposome modification improved biocompatibility and systemic stability. At the tumor site, the AML system enabled controlled anlotinib release and ROS generation via Fe-mediated Fenton-like reactions, producing synergistic anti-tumor effects. The AML system integrates ROS generation with targeted therapy, providing new insights for lung cancer treatment.

Data Sharing Statement

Data supporting the findings of this study are available from Prof. Yu Huo upon reasonable request.

Ethics Approval

All animal procedures were approved by the Experimental Animal Ethics Committee of Guangxi University of Chinese Medicine (DW20230528-104) and were performed in accordance with the Guide for the Care and Use of Laboratory Animals published by the National Institutes of Health (NIH).

Acknowledgments

The authors would like to extend sincere thanks to Yu Huo for his generous support in providing essential reagents that were crucial to the success of this research.

Author Contributions

All authors made a significant contribution to the work reported, whether that is in the conception, study design, execution, acquisition of data, analysis and interpretation, or in all these areas; took part in drafting, revising or critically reviewing the article; gave final approval of the version to be published; have agreed on the journal to which the article has been submitted; and agree to be accountable for all aspects of the work.

Funding

The present study was funded by National Key R&D Program of China (grant nos. 2023YFC2508601, 2023YFC2508604 and 2023YFC2508605), Tongji University Medicine-X Interdisciplinary Research Initiative (grant no. 2025-0554-ZD-08), Shanghai Hospital Development Center Foundation (grant no. SHDC22025208), Shanghai Hospital Development Center Foundation (grant no. SHDC12024125), Clinical Research Foundation of Shanghai Pulmonary Hospital (grant no. LYRC202401), Innovation Team Project of the Faculty of Chinese Medicine Science, Guangxi University of Chinese Medicine (grant nos. 2023CX001 and 2024ZZA004).

Disclosure

The author(s) report no conflicts of interest in this work.

References

1. Osborne JK, Minna JD. Lung cancer cell of origin: controversy and clinical translational implications. *Cancer Res*. 2022;82(6):972–973. doi:10.1158/0008-5472.can-22-0301
2. Pennycuick A, Janes SM. On the origin of lung cancers. *Am J Respir Crit Care Med*. 2020. doi:10.1164/rccm.201911-2176ed
3. Tang W-F, Wu M, Bao H, et al. Timing and origins of local and distant metastases in lung cancer. *J Thorac Oncol*. 2021. doi:10.1016/j.jtho.2021.02.023
4. Oser MG, Niederst MJ, Sequist LV, Engelman JA. Transformation from non-small-cell lung cancer to small-cell lung cancer: molecular drivers and cells of origin. *Lancet*. 2015. doi:10.1016/s1470-2045(14)71180-5.
5. Sutherland Kate D, Proost N, Brouns I, Adriaensen D, Song J-Y, Berns A. Cell of origin of small cell lung cancer: inactivation of Trp53 and Rb1 in distinct cell types of adult mouse lung. *Cancer Cell*. 2011. doi:10.1016/j.ccr.2011.04.019
6. Giaccone G, He Y. Current knowledge of small cell lung cancer transformation from non-small cell lung cancer. *Semi Cancer Biol*. 2023. doi:10.1016/j.semcancer.2023.05.006
7. Tang W-F, Fu R, Liang Y, et al. Genomic evolution of lung cancer metastasis: current status and perspectives. *Cancer Commun*. 2021. doi:10.1002/cac2.12237
8. Miller M, Hanna N. Advances in systemic therapy for non-small cell lung cancer. *BMJ*. 2021;375:n2363. doi:10.1136/bmj.n2363
9. Chaft JE, Shyr Y, Sepesi B, Forde PM. Preoperative and postoperative systemic therapy for operable non-small-cell lung cancer. *J Clin Oncol*. 2022;40(6):546–555. doi:10.1200/jco.21.01589
10. Temel JS, Petrillo LA, Greer JA. Patient-centered palliative care for patients with advanced lung cancer. *J Clin Oncol*. 2022;40(6):626–634. doi:10.1200/jco.21.01710
11. Wang M, Herbst RS, Boshoff C. Toward personalized treatment approaches for non-small-cell lung cancer. *Nat Med*. 2021;27(8):1345–1356. doi:10.1038/s41591-021-01450-2
12. Hirsch FR, Scagliotti GV, Mulshine JL, et al. Lung cancer: current therapies and new targeted treatments. *Lancet*. 2017;389(10066):299–311. doi:10.1016/s0140-6736(16)30958-8
13. Lahiri A, Maji A, Potdar PD, et al. Lung cancer immunotherapy: progress, pitfalls, and promises. *Mol Cancer*. 2023;22(1):40. doi:10.1186/s12943-023-01740-y
14. Cheng Y, Chen J, Zhang W, et al. Benmelstobart, anlotinib and chemotherapy in extensive-stage small-cell lung cancer: a randomized Phase 3 trial. *Nature Med*. 2024. doi:10.1038/s41591-024-03132-1
15. Lian Z, Du W, Zhu J, Zeng Y, Liu Z, Huang JA. 129PAnlotinib can overcome acquired resistance to EGFR-TKIs via FGFR1 signaling in non-small cell lung cancer. *Ann Oncol*. 2019. doi:10.1093/annonc/mdz063.027
16. Lu J, Zhang W, Yan B, et al. 368OTumor mutation index as a biomarker for responsive stratification on multi-targeted TKI anlotinib: an ALTER-0303 companion diagnostic study. *Ann Oncol*. 2018. doi:10.1093/annonc/mdy441.001
17. Sun Y, Niu W, Du F, et al. Safety, pharmacokinetics, and antitumor properties of anlotinib, an oral multi-target tyrosine kinase inhibitor, in patients with advanced refractory solid tumors. *J Hematol Oncol*. 2016. doi:10.1186/s13045-016-0332-8
18. Zhuang H, Wang Y, Cheng C, Shi S. The efficacy of anlotinib instead of glucocorticoids for edema induced by brain metastases in NSCLC patients with anti-PD1/PDL-1 immunotherapy. *Neuro-Oncology*. 2020. doi:10.1093/neuonc/noaa236

19. Zhu H, Jia W, Jing X, Huang W, Wang L, Yu J. Severe pulmonary toxicity with concurrent anlotinib and chemoradiotherapy in Stage III NSCLC: the ALTER-L042 Phase 1 clinical trial. *JTO Clin Res Rep*. 2022;3(6):100339. doi:10.1016/j.jtocrr.2022.100339
20. Shen G, Zheng F, Ren D, et al. Anlotinib: a novel multi-targeting tyrosine kinase inhibitor in clinical development. *J Hematol Oncol*. 2018;11 (1):120. doi:10.1186/s13045-018-0664-7
21. Li S, Wang H. Research progress on mechanism and management of adverse drug reactions of anlotinib. *Drug Des Devel Ther*. 2023;17:3429–3437. doi:10.2147/dddt.S426898
22. Lian X, Fang Y, Joseph E, et al. Enzyme–MOF (metal–organic framework) composites. *Chem Soc Rev*. 2017. doi:10.1039/c7cs00058h
23. Yang F, Dong J, Li Z, Wang Z. Metal–organic Frameworks (MOF)-assisted sonodynamic therapy in anticancer applications. *ACS Nano*. 2023. doi:10.1021/acsnano.2c10251
24. Younis SA, Bhardwaj N, Bhardwaj SK, Kim K-H, Deep A. Rare earth metal–organic frameworks (RE-MOFs): synthesis, properties, and biomedical applications. *Coord Chem Rev*. 2020. doi:10.1016/j.ccr.2020.213620
25. Ruoyu C, Lingxi J, Han G, et al. A pH-responsive cluster metal-organic framework nanoparticle for enhanced tumor accumulation and antitumor effect. *Adv Mater*. 2022;34(42). doi:10.1002/adma.202203915
26. Wang C, Jia X, Zhen W, Zhang M, Jiang X. Small-sized mof-constructed multifunctional diagnosis and therapy platform for tumor. *ACS Biomater Sci Eng*. 2019. doi:10.1021/acsbiomaterials.9b00813
27. Eguchi M, Hirata S, Ishigami I, et al. Pre-treatment of oncolytic reovirus improves tumor accumulation and intratumoral distribution of PEG-liposomes. *J Control Release*. 2023. doi:10.1016/j.jconrel.2022.12.050
28. n N, n U, n K. The size of liposomes: a factor which affects their targeting efficiency to tumors and therapeutic activity of liposomal antitumor drugs. *Adv Drug Delivery Rev*. 2000. doi:10.1016/s0169-409x(99)00041-1
29. Saito S, Nakashima I, Hasegawa A, et al. Tumor-tropic liposome-mediated therapeutic delivery of mRNA for T cell malignancies. *Blood*. 2020. doi:10.1182/blood-2020-139020
30. Wang G, Wu B, Li Q, et al. Active transportation of liposome enhances tumor accumulation, penetration, and therapeutic efficacy. *Small*. 2020. doi:10.1002/smll.202004172
31. Ji T, Lang J, Wang J, et al. Designing liposomes to suppress extracellular matrix expression to enhance drug penetration and pancreatic tumor therapy. *ACS Nano*. 2017. doi:10.1021/acsnano.7b01026
32. Lu Y-J, Chuang E-Y, Cheng Y-H, Anilkumar TS, Chen H-A, Chen J-P. Thermosensitive magnetic liposomes for alternating magnetic field-inducible drug delivery in dual targeted brain tumor chemotherapy. *Chem Eng J*. 2019. doi:10.1016/j.cej.2019.05.055
33. Pitchaimani A, Nguyen TDT, Aryal S. Natural killer cell membrane infused biomimetic liposomes for targeted tumor therapy. *Biomaterials*. 2018. doi:10.1016/j.biomaterials.2018.01.018
34. Wang D-Y, Yang G, van der Mei HC, Ren Y, Busscher HJ, Shi L. Liposomes with water as a pH-responsive functionality for targeting of acidic tumor and infection sites. *Angew Chem Int Ed*. 2021. doi:10.1002/anie.202106329
35. Mi Y, Chen Y, Gu G, et al. New synthetic Adriamycin-incorporated chitosan nanoparticles with enhanced antioxidant, antitumor activities and pH-sensitive drug release. *Carbohydr Polym*. 2021. doi:10.1016/j.carbpol.2021.118623
36. Pan D, Chen K, Zhou Q, et al. Engineering of CdTe/SiO2 nanocomposites: enhanced signal amplification and biocompatibility for electrochemi-luminescent immunoassay of alpha-fetoprotein. *Biosens Bioelectron*. 2019. doi:10.1016/j.bios.2019.02.022
37. Meng Y, Wang Y, Wang S, et al. Direct solvent-derived polymer-coated nitrogen-doped carbon nanodots with high water solubility for targeted fluorescence imaging of glioma. *Small*. 2015. doi:10.1002/smll.201403718
38. Wenxiu Y, Maotuan H, Wenqian C, et al. Reduced graphene oxide loaded with tetrahedral framework nucleic acids for combating orthodontically induced root resorption. *J Nanobiotechnol*. 2024. doi:10.1186/s12951-024-02988-2
39. Chang M, Wei Y, Liu D, Wang J-X, Chen J-F. A general strategy for instantaneous and continuous synthesis of ultrasmall metal–organic framework nanoparticles. *Angew Chem Int Ed*. 2021. doi:10.1002/anie.202112250
40. Chen Z, Li Z, Tang N, et al. Engineering ultra-small cerium-based metal–organic frameworks nanozymes for efficient antioxidative treatment of dry eye disease. *Adv Funct Mater*. 2023. doi:10.1002/adfm.202307569
41. Dai S, Simms C, Patriarche G, et al. Highly defective ultra-small tetravalent MOF nanocrystals. *Nat Commun*. 2024. doi:10.1038/s41467-024-47426-x
42. Ma Y, Su Z, Zhou L, et al. Biodegradable metal-organic-framework-gated organosilica for tumor-microenvironment-unlocked glutathione-depletion-enhanced synergistic therapy. *Adv Mater*. 2022;34(12):e2107560. doi:10.1002/adma.202107560
43. Alneghery LM, Al-Zharani M, Nasr FA, et al. Fabrication and optimization of naringin-loaded MOF-5 encapsulated by liponiosomes as smart drug delivery, cytotoxicity, and apoptotic on breast cancer cells. *Drug Dev Ind Pharm*. 2025;51(9):1016–1029. doi:10.1080/03639045.2024.2388786
44. Karami A, Ahmed A, Sabouni R, et al. Hybrid liposome/metal-organic framework as a promising dual-responsive nanocarriers for anticancer drug delivery. *Colloids Surf B Biointerfaces*. 2022;217:112599. doi:10.1016/j.colsurfb.2022.112599